

# All-optical photonic switch via the higher-order topological spin Hall effect

Evelyn Y. González-Ramírez<sup>1,2,\*</sup>, José G. Murillo-Ramírez<sup>1,2</sup>, Óscar O. Solís-Canto<sup>1,2</sup>, and José A. Medina-Vázquez<sup>1,2</sup>

<sup>1</sup>*Centro de Investigación en Materiales Avanzados S.C., Complejo Industrial Chihuahua, Miguel de Cervantes 120  
C.P. 31136, Chihuahua, Chih., Mexico*

<sup>2</sup>*Facultad de Ingeniería, Universidad Autónoma de Chihuahua, Nuevo Campus Universitario, Circuito,  
Universitario S/N 31125, Chihuahua, Chih., Mexico*



(Received 6 December 2023; revised 24 February 2024; accepted 5 April 2024; published 19 April 2024)

Topological photonics has established itself as a promising area for the development of photonic integrated circuits due to the robust properties of topological states. In recent years, different logical devices have been proposed to form the fundamental elements of an integrated topological photonic circuit. Despite the rapid theoretical growth of topological photonics, it still lacks experimental foundations concerning logical devices for on-chip integration. For this reason, in this work, we report the design and build of an all-optical photonic switch in a silicon slab working under the higher-order topological spin Hall effect. We have taken advantage of the gapped edge states due to the higher-order topology and combined this feature with changes in the dielectric permittivity of silicon by inducing transitions of free charge carriers. The transitions of charge carriers were realized through the incidence of electromagnetic radiation with a frequency close to the visible-ultraviolet region boundary, making the device operation entirely optical. The behavior of the constructed device has also been numerically simulated and compared with the experimental results obtained. This work contributes to the idea that photonic crystals are a powerful platform for studying topological states and paves the way for the experimental realization of integrated topological optical circuits.

DOI: [10.1103/PhysRevApplied.21.044038](https://doi.org/10.1103/PhysRevApplied.21.044038)

## I. INTRODUCTION

Light guiding is a topic of great interest due to the possibility of obtaining photonic integrated circuits. Unfortunately, conventional waveguides often present problems of losses during the propagation over long distances or sudden changes in the direction of propagation. Photonic crystals (PhCs), capable of operating at relatively high frequencies in the ranges of near-infrared (telecommunications) and visible light, solve so much of the losses in signal transmission caused by conventional methods because they work efficiently with guided modes usually located within a photonic band gap [1–3]. Due to the existence of the band gap, the guiding of a light beam is straightforward for different propagation directions by introducing linear structural defects [4–9]. Nevertheless, PhCs usually present undesirable fabrication defects because it is difficult to have control of the manufacturing process. In this sense, the fabrication defects compromise the confinement of light within the waveguide, causing undesired radiative modes that induce light loss in the PhC. Despite this, PhCs are still a solution to overcome losses in light beam propagation.

The recent employment of topological concepts in crystal structures has led to the development of the topological photonics that can solve these undesirable losses in light propagation, allowing robust guided modes even under severe perturbations [10–16]. These robust states occurring at the boundaries of the structure are due to global topological properties across the momentum space, known as the bulk-boundary correspondence [17]. Topological photonics studies the behavior of the photon wave function in a photonic band structure and grew out of the similarities of photonic crystals with solid-state physics [18–24]. Like topological insulators in solid-state physics, photonic topological insulators occur in periodic materials with a band gap, whose bulk bands exhibit a distinct topological invariant [17,25].

One of the most fascinating offerings of topological photonics is the possibility of invoking the pseudospin degree of freedom of photons [26–30] and combining it with the nontrivial band topology. In this way, the propagation of light can be enabled unidirectionally and without the occurrence of dissipation and backscattering. This recently discovered phenomenon is known as the quantum spin Hall effect (QSHE) of light [31–33]. In this class of topological phases, boundary states characterized by a topological invariant are found and support spin-boundary

\*Corresponding author: evgonzalez@uach.mx

transport, which leads to the development of spin-photonic devices [19,34–41].

In recent years, another class of topological phases of matter has been introduced, which has the ability to generate an unconventional bulk-edge-corner correspondence [42]. This topological phase is known as the higher-order topological insulator (HOTI) phase. In the HOTI phase, the generalized bulk-edge-corner correspondence allows us to find topological states confined at the boundaries, known as corner states [42–45]. Moreover, the higher-order feature allows locating edge states inside the band gap to be gapped [46,47]. Thus, in the higher-order topological spin Hall (HOTSH) phase, gapped edge states are spectrally isolated from the bulk states and have spinful properties that enable unidirectional propagation. For this reason, the HOTSH effect is of great experimental interest due to topological robustness that provides both spectrally isolated gapped edge states (of the rest of the bulk states) and a unidirectional or partially unidirectional transport of these guided modes. Furthermore, a significant interest in systems with the topological spin Hall effect has increased in recent years due to the possibility of integrating it into devices compatible with other technologies of interest. Despite the great virtues offered by the HOTSH effect, very few studies have been performed in this regard, and its integration with other technologies is still quite limited.

On the other hand, in recent studies, a charge-carrier transition has been induced in semiconductor materials by illumination with light of a frequency close to the energy band gap of a semiconductor material [48]. This induction of free charge carriers changes the dielectric permittivity of the irradiated material due to an increment in its electric conductivity [49]. Because of the vast applications of silicon (Si) devices, it is common its use in the generation of changes in the dielectric permittivity by illumination with light whose wavelength is near the border of the ultraviolet-visible (UV-vis) spectrum, on the order of 400 nm [48,49]. In this way, alternative devices have been proposed that allow dielectric permittivity change-dependent operation with promising applications in photonic integrated circuits [50].

Because of the benefits provided by topological photonics, we have designed and experimentally constructed a HOTSH PhC with gapped edge states and optical switch behavior by means of sufficiently energetic illumination to induce charge-carrier transitions from the conduction band to the valence band. The HOTSH PhC has been designed based on the Su-Schrieffer-Heeger (SSH) model due to its well-known versatility in generating topological phase transitions. Subsequently, we identified the edge states in the topological PhC at a wavelength of 1550 nm by first-principles calculations and then performed its experimental construction based on the proposed theoretical model. The fabrication of the PhC was performed entirely by the

focused-ion-beam (FIB) milling method since this method allows the building of the photonic structure in a single production process. Next, the optical characterization of the PhC was carried out by coupling an infrared laser beam at the interface of the HOTSH PhCs formed by two PhC with distinct topological invariants. This coupling process occurs because the wavelength of the incident laser coincides with the wavelength corresponding to the edge state previously predicted by numerical simulation. Once we experimentally confirmed the presence of the edge state, we proceeded to characterize the structure under a bath of noncoherent violet light. The results of this characterization revealed that the change in dielectric permittivity, and consequently in the refractive index, is sufficient to shift the frequency of the edge state. Therefore, the incident infrared laser can no longer be coupled to the photonic structure as an edge state under the violet radiation bath. These results demonstrate that it is feasible and straightforward to connect the virtues of photonic topological insulators with the dynamic modulation offered by the induction of free charge-carrier transitions employing incident energetic radiation. Furthermore, our results expand the fundamentals and the state of the art in the experimental fabrication of topological photonic devices for future applications in different types of integrated photonic circuits.

## II. DESIGN

The design of our HOTSH PhC was based on the SSH model [51], with a hexagonal lattice. To mimic the SSH model we selected two unit cells from a hexagonal PhC slab with square air holes, as shown in Fig. 1(a). This selection of unit cells mimics quite well the intra- and intercell interactions between nearest neighbors described in the SSH model. All theoretical calculations were performed through numerical simulations using the finite-element method (FEM) and the commercial software COMSOL Multiphysics. The master equation

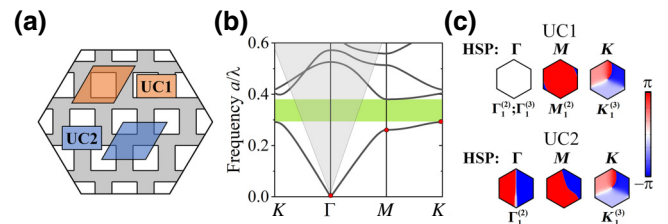


FIG. 1. Design of the HOTSH PhC. (a) Selection of unit cells UC1 and UC2 describing a triangular mesh of square air holes. (b) Photonic band diagram obtained from UC1 and UC2. Both unit cells produce the same band diagram. The gray region represents the light cone. (c)  $H_2$  magnetic field phase profiles of the photonic Bloch functions below the band gap in the HSPs for UC1 and UC2.

of the harmonic modes is derived from Maxwell's equations,  $[\nabla^2 + (\omega^2/c^2)\varepsilon(\mathbf{r})]\mathbf{E} = 0$  being  $\varepsilon(\mathbf{r})$  the position-dependent permittivity and  $c$  is the speed of light. The magnetic field is obtained from the Faraday relation  $\mathbf{H} = -[i/\mu_0\omega]\nabla \times \mathbf{E}$ , where the permeability  $\mu_0$  is that of the vacuum. The structural parameters of the PhC consist of a lattice parameter  $a$ , square hole side of  $L = 0.5a$ , slab thickness  $t = 1.4a$  and the dielectric permittivity used was that of Si,  $\varepsilon_{\text{Si}} = 12.05$  [52]. In the experimental fabrication of the topological PhC, we chose a lattice parameter  $a = 0.5 \mu\text{m}$  with the aim of locating the topological states frequencies at the near-infrared region, close to the communication bands. Figure 1(b) shows the photonic band diagram corresponding to the unit cell UC1 selected and marked in Fig. 1(a), revealing a rather wide photonic band gap. By selecting a different unit cell (UC2), such as the one shown in Fig. 1(a), one obtains a photonic band structure identical to the band structure of the original unit cell UC1 [see Fig. 1(b)]. However, the topological invariants of both band structures determine whether they are topologically equivalent.

Crystalline symmetry plays a fundamental role in the manifestation of a topological band gap. For this reason, we have used the symmetry eigenvalues at the high symmetry points (HSPs) in the first Brillouin zone to characterize the topology of the bands and, in particular, the topology of the band gap. Figure 1(c) shows the phase profiles of the magnetic field distribution ( $H_z$ ) as the magnetic field emulates the Berry curvature in photonic crystals [25].

The different selection of the unit cell in the lattice of square air holes introduces an additional degree of freedom regarded as a pseudospin, under the constraint that the system has a  $C_{6v}$  symmetry point group and reversible time symmetry. Subsequently, based on the eigenvalues of the  $C_6$  operation on the HSPs, the topological classification of the photonic crystal can be performed from the rotation symmetries and the eigenvalues of the rotation operation. The eigenvalues of these rotation operations are taken in the HSPs ( $\Pi = M, K$ ), being [42]

$$\Pi_p^{(n)} = e^{2\pi i(p-1)/n} \quad \text{for } p = 1, 2, \dots, n. \quad (1)$$

From these eigenvalues, we can define the following integer invariants:

$$[\Pi_p^{(n)}] = \#\Pi_p^{(n)} - \#\Gamma_p^{(n)}, \quad (2)$$

where  $\#\Pi_p^{(n)}$  is the number of states in the photonic bands in question with rotation operation eigenvalue  $\Pi_p^{(n)}$ . Leaving aside some redundant invariants appearing in Eq. (2), the resulting topological classification in the photonic

crystal with  $C_6$  symmetry is given as follows [42,46,47]:

$$\chi^{(6)} = \left( \left[ M_1^{(2)} \right], \left[ K_1^{(3)} \right] \right). \quad (3)$$

The corresponding required values of Eq. (3) are acquired from the phase profile shown in Fig. 1(c), under the eigenvalues of the rotation operation. Therefore, the topological classification results for UC1  $\chi^{(6)} = (0, 0)$  and for UC2  $\chi^{(6)} = (-1, 1)$ , which leaves UC2 classified as the non-trivial structure. It is worthwhile to note that the photonic crystals described by UC1 and UC2 with different topological indices belong to different topological classes. For this reason, they cannot be deformed from one to the other unless the bulk band gap is closed or the  $C_6$  symmetry is broken, which is precisely what happens at an interface formed by these two PhCs.

Additionally, the configuration of the PhC can lead to a higher-order topological character. This higher-order character is directly related to the invariant of the bulk topology, so we can define a higher-order topological corner charge as follows [42,46,47]:

$$Q_{\text{corner}}^{(6)} = \frac{1}{4} \left[ M_1^{(2)} \right] + \frac{1}{6} \left[ K_1^{(3)} \right], \quad (4)$$

which is calculated in a similar manner to the calculation of the topological invariant  $\chi^{(6)}$ . As a result, it is obtained that the trivial cell UC1 has a  $Q^{(6)} = 0$  and the nontrivial cell UC2 has a  $Q^{(6)} = -1/12$ . Such nontrivial corner indices indicate the emergence of corner states and consequently the proof that the system is in the higher-order topological phase.

Taking into account the previously performed analysis, we combine the PhCs obtained with UC1 and UC2 to form domain walls that support edge states. As shown in Fig. 2(a), the interface between PhC<sub>UC1</sub> and PhC<sub>UC2</sub> results in a domain wall, which can be analyzed by extracting a supercell. In this analysis, we used a  $10 \times 1$  supercell [as shown in the first panel of Fig. 2(b)] and subsequently imposed Floquet periodic boundary conditions on the left and right edges of the supercell. At the upper and lower boundaries of the supercell we placed scattering conditions. The panels at the right of Fig. 2(b) show, respectively, the  $|H_z|$  field and phase distribution for a localized eigenstate at the HOTSH PhC interface. In addition, we obtained the vector field describing the Poynting vector  $\mathbf{S} = \text{Re}[\mathbf{E} \times \mathbf{H}^*]/2$ . The vector field distribution describing the Poynting vector in the supercell shows the vortices of a pseudospin generated at the topological interface, which indicates the presence of the spin Hall effect in the HOTI phase. We then constructed the band diagram projection for the supercell shown in Fig. 2(c), where it can be seen that has appeared, within the photonic band gap, an edge band belonging to the edge state. This edge band is gapped, where the higher-order topology facilitates

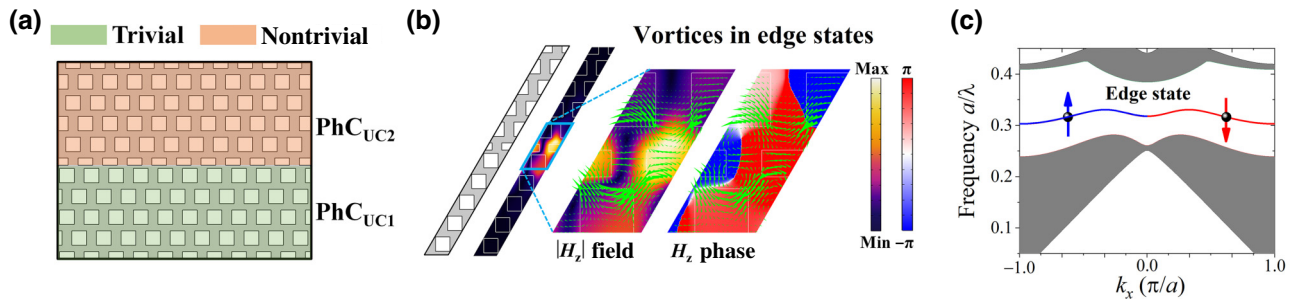


FIG. 2. (a) Interface formed by PhC<sub>UC1</sub> and PhC<sub>UC2</sub>, creating a domain wall. (b)  $10 \times 1$  supercell, containing the topological interface. On the right is shown the distribution of the  $|H_z|$  field in the supercell and the  $H_z$  phase distribution. The inset highlights the presence of the Poynting vector vortices visualized by green arrows. (c) Projection of the photonic band diagram obtained with the supercell designed. By means of the vortex distribution of the Poynting vectors, we found the different pseudospin configurations of the band with edge states. The blue upward arrow indicates a positive upward pseudospin and the red arrow indicates a negative downward pseudospin.

the existence of gapped edge states due to the breaking of  $C_6$  symmetry at the edges. Since no edge preserves  $C_6$  symmetry, gapped opening is inevitable in the edge states [46,47,51]. Furthermore, using the distribution of the Poynting vectors, we can identify the pseudospin freedom degree of the edge band. We have identified the positive pseudospin in the band diagram with a blue up arrow and the negative pseudospin with a red down arrow, as shown in Fig. 2(c).

Once we obtained the topological properties and identified the presence of the gapped edge states, we proceeded to find these states in the complete HOTSH PhC, formed by the PhCs obtained with UC1 and UC2. In the calculation of the eigenfrequencies in the HOTSH PhC, we found the edge states with unidirectional propagation, due to the presence of the pseudospin freedom degree. The edge states exhibiting this feature are shown

in Fig. 3(a) ( $|H_z|$  field distribution), where it is illustrated that a positive pseudospin favors a rightward unidirectional propagation, and a negative pseudospin favors a leftward propagation.

In order to give a conclusive proof that the system is in the higher-order topological spin Hall phase, we show the corner states that appear if a topological corner is formed. Figure 3(b) shows the corner interface, constructed from the trivial UC1 and nontrivial UC2 unit cells. We compute the eigenstates that exist in the HOTSH PhC with the topological corner as shown in Fig. 3(c). The inset in Fig. 3(c) shows the  $|H_z|$  distribution of the field in the topological corner, revealing the existence of the confined corner state in that region, predicted by the topological index  $Q^{(6)} = -1/12$ . An in-depth experimental study of the corner states present in our HOTSH PhC is outside the scope of this paper.

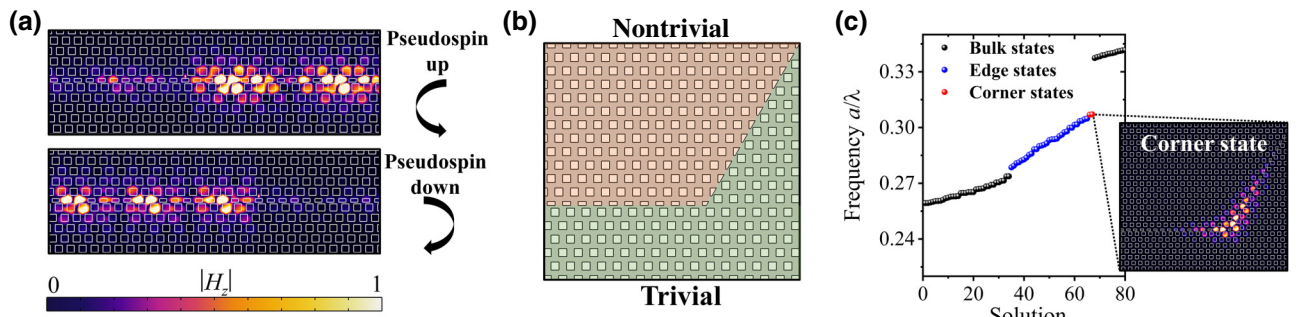


FIG. 3. (a)  $|H_z|$  field distribution calculated, corresponding to gapped edge states with pseudospin character at the topological interface of HOTSH PhC. The upper panel indicates the propagation of the edge state with a positive pseudospin, while the lower panel shows the propagation of an edge state with a negative pseudospin. (b) Topological corner design formed from two PhCs, one with trivial UC1 and the other with nontrivial UC2. (c) Eigenfrequencies computed in the HOTSH PhC with the topological corner. Both edge states and corner states are indicated. The inset shows the distribution of the  $|H_z|$  field corresponding to the corner state presented in the HOTSH PhC, highlighting the higher-order topological character. All field distributions were calculated on the silicon slab with a thickness of  $0.7 \mu\text{m}$ .

### III. RESULTS

Having numerically confirmed the presence of a gapped edge state in the proposed photonic structure, we experimentally verified the existence of these topological states. The HOTSH PhC was fabricated on a Si slab, where the whole fabrication process was done by the milling method via a FIB using gallium ions. The fabrication was performed in two steps: first, a box was milled on the border of a monocrystalline Si substrate. Prior to this milling, a polishing process was performed on the edge of the Si substrate. Figure 4(a) shows a schematic representation of the box fabrication process on the Si substrate and Fig. 4(b) shows a SEM micrograph of the box-shaped milling. The top of the Si box comprises the slab on which the square air holes forming the HOTSH PhC will be milled. This slab has structural parameters corresponding to a thickness of 700 nm and a width of 20  $\mu\text{m}$ . In the second fabrication step, we rotate the Si sample and proceed with the air holes milling. Figure 4(c) shows the SEM micrograph of the square air hole pattern milled in the Si slab. Here, the operating parameters of the FIB were a dose of 1.5 nC/ $\mu\text{m}^2$  and a current of 10 pA. These parameters allowed for preserving the square geometry of the air holes with the dimensions that reproduce the theoretical calculations.

The device built was characterized using the experimental setup shown schematically in Fig. 5(a). As a light source, we used a highly monochromatic butterfly laser with a wavelength of 1550 nm, which matches the mode of the gapped edge state found in the numerical simulations. The laser radiation was cleaned by a spatial filter and then focused by a convex lens with a focal length of 15 mm, achieving a beam waist size of 10  $\mu\text{m}$ . The sample was placed in a mount with 6 degrees of freedom, to achieve precise positioning of the HOTSH PhC sample. Subsequently, we focused the laser light at one end of the HOTSH PhC interface and placed a low-power infrared radiation detector near the opposite end of the interface. By placing it perpendicular to the incident beam, we are

neglecting most of the reflected and scattered radiation from the sample, thus maximizing the detection of the coupled light into the PhC. In order to confirm the existence of the gapped edge state and to observe the spatial coordinate at which the maximum coupling of incident radiation occurs at the interface of the PhC, we made a spatial sweep of incidence on the PhC along the  $y$  coordinate as shown in Fig. 5(b). As expected, the highest coupling occurs when the beam is directly incident at the topological interface, as shown in the red dots curve of Fig. 5(c). We compare the coupling curve with a curve obtained theoretically from numerical simulations shown in Fig. 5(d) with a continuous red line.

After confirming the existence of the edge state, we proceeded to illuminate the device with incoherent radiation near the border of the UV-vis spectrum. The device was illuminated by using a light-emitting diode (LED) with an emission centered at a wavelength of 400 nm. A light beam with this wavelength has sufficient energy to induce a transition of charge carriers to the conduction electronic band in Si and in consequence a slight change in its refractive index due to an increment in the electric conductivity caused by the increase in the charge-carrier density. Hence, the edge state is no longer at the same wavelength as in the case without 400-nm LED illumination. Regarding the principle of operation, Si has an energy band gap of about 1.14 eV, equivalent to the energy of a photon with a wavelength of 1.1  $\mu\text{m}$ . When the light incident on Si has an energy equal to or greater than the energy range of the band gap, electrons from the valence band can experience a transition to the conduction band. In this work, we have used the Drude model to describe the variation of dielectric permittivity  $\Delta\epsilon_{\text{FC}}$  under illumination [53]:

$$\Delta\epsilon_{\text{FC}} = - \left[ \frac{\omega_p(F_{\text{eff}})}{\omega} \right]^2 \frac{1}{1 + i(1/\omega\tau_D)}, \quad (5)$$

where  $\omega$  is the angular frequency of the incident beam,  $F_{\text{eff}}$  is the effective pump fluence,  $\tau_D$  is the Drude damping

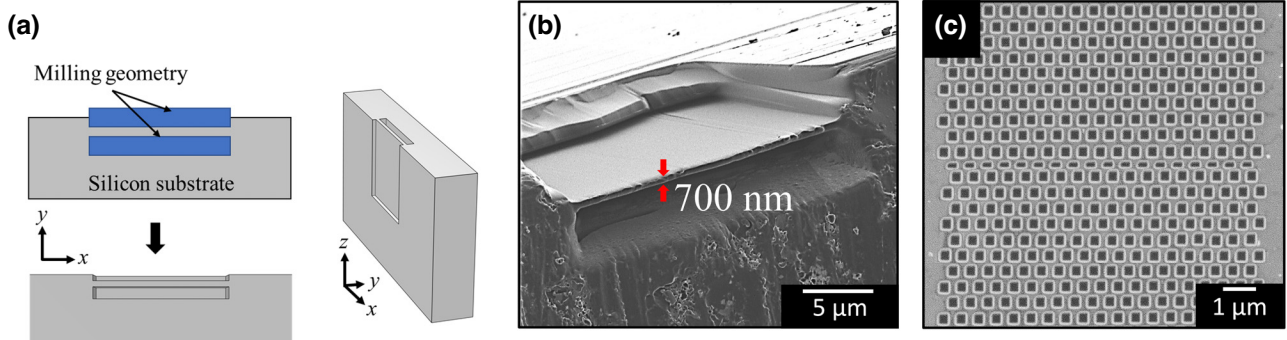


FIG. 4. (a) Schematic representation of the Si slab fabrication process from a box-shaped geometry. The blue-shaded regions denote the volume of material removed by FIB machining. (b) SEM micrograph of the Si plate obtained by box-shaped machining. (c) SEM micrograph of the topological PhC formed with a hexagonal lattice and square air holes.

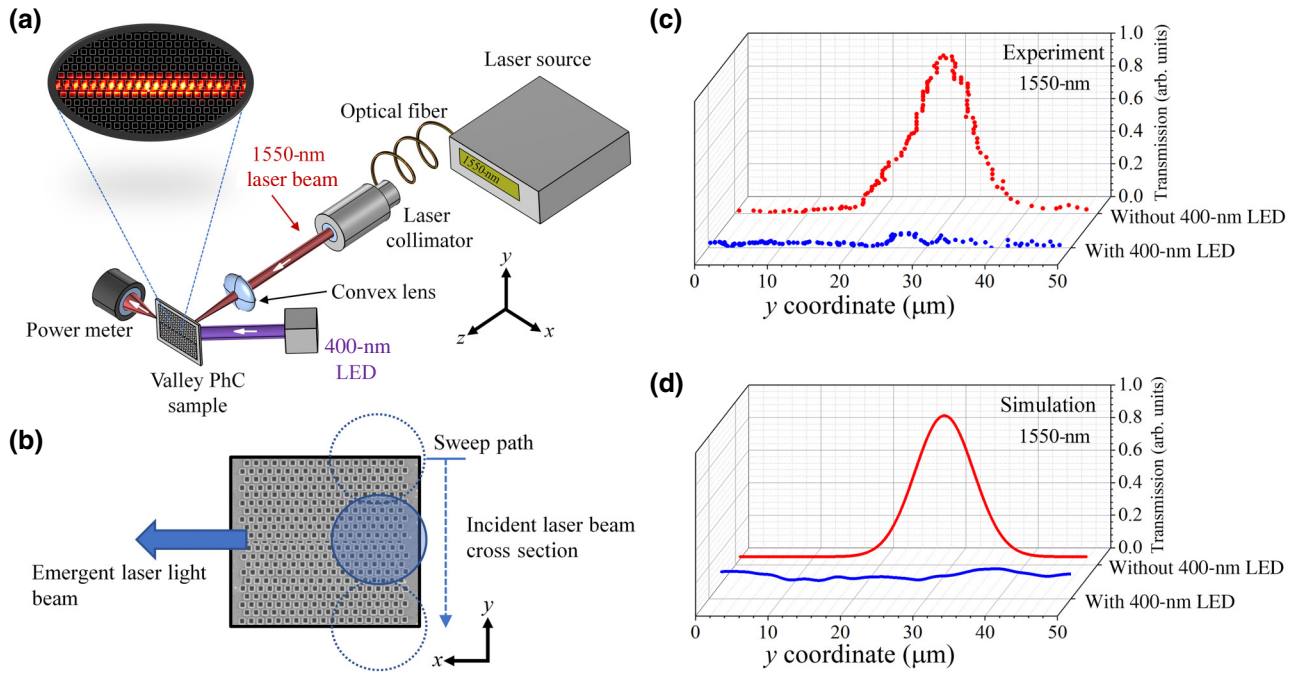


FIG. 5. (a) Representation of the experimental configuration used to measure the edge state in the HOTSH PhC. A butterfly laser diode attached to a single-mode optical fiber is coupled to an optical collimator. Subsequently, the laser beam is focused with a convergent lens to incidence on the sample. The coupled light beam travels at the interface HOTSH PhC and exits to be measured by a low-power detector. (b) A spatial scan process along the  $y$  coordinate is performed to demonstrate the existence of the edge state. The maximum coupling occurs when the laser beam approaches the interface HOTSH PhC. (c) Experimental measurement of the amplitude of coupled and guided light beam emerging from the topological PhC as a function of the spatial coordinate  $y$  in which the laser beam was swept. The red dots show the intensity of the laser beam obtained after traveling through the topological interface without the incidence of the LED pump incoherent beam. The blue dots correspond to the amplitude of coupled and guided emergent coherent light beam through the topological PhC, with the light bath provided by the pumping incoherent beam with the 400-nm LED. (d) Theoretical transmission of the coupled light beam obtained from numerical simulations where the continuous red line denotes the intensity of the laser beam of 1550 nm coming from the topological interface and without the LED pumping incoherent beam. The continuous blue curve is the transmission of the laser beam of 1550 nm coming from the topological interface under the bath of the pump light beam of the LED at 400 nm.

time, and  $\omega_p(F_{\text{eff}})$  is the plasma frequency defined as

$$\omega_p(F_{\text{eff}}) = \sqrt{\frac{N_{e-h}(F_{\text{eff}})e^2}{\varepsilon_0 m_{\text{opt}}^* m_e}} \quad (6)$$

Here,  $m_{\text{opt}}^* = (1/m_e^* + 1/m_h^*)^{-1}$  is the dimensionless optical effective mass of the charge carrier,  $N_{e-h}(F_{\text{eff}})$  denotes the electron-hole density as a function of the pump fluence, and  $\varepsilon_0$  stands for the vacuum permittivity.

The electron density  $N_{e-h}(F_{\text{eff}})$  in Eq. (6) is described by the following equation [53]:

$$N_{e-h}(F_{\text{eff}}) = \frac{F_{\text{eff}}}{\hbar\omega} \left( \alpha + \beta \frac{F_{\text{eff}}}{2t_0\sqrt{2\pi}} \right), \quad (7)$$

where  $\alpha$  is the linear absorption coefficient,  $\beta$  is the two-photon absorption coefficient,  $t_0$  is the pump-pulse duration, and  $\hbar$  is the reduced Planck constant. The first term of the electron density equation tends to have a much more

relevant contribution when the system is subjected to low levels of pump fluence, since the second term is subject to the square of the pump fluence. This is true for our case because the pumped fluence is approximately  $17.5 \text{ mJ/cm}^2$ . Additionally, the  $\beta$  coefficient, related to nonlinear processes, is several orders of magnitude smaller than the linear coefficient  $\alpha$  in silicon. This is also true for materials that do not have significant nonlinear behavior. For this reason, the second term of Eq. (7) can be neglected. Substituting the result of the reduced Eq. (7), in Eq. (6), we obtain,

$$\omega_p(F_{\text{eff}}) = \sqrt{\frac{F_{\text{eff}}\alpha e^2}{\hbar\omega\varepsilon_0 m_{\text{opt}}^* m_e}}. \quad (8)$$

Then, with the plasma frequency in Eq. (8), we can relate the change of dielectric permittivity to the effective pumping fluence and electron density of silicon under incoherent illumination. This results in a linear dependence of the change in refractive index on the beam fluence,

and if the refractive index change is small, it can be approximated as  $\Delta n = \Delta\epsilon/(2n)$ . Using this value of the pumped fluence and typical values in Si of the Drude damping time  $\tau_D = 10^{-14}$  s, and the electron-hole density  $N_{e-h} = 10^{19}$  cm<sup>3</sup> [53,54], we obtained a refractive index change of  $-0.02$ , which is in agreement with different experimental values obtained in the literature [50–54].

The next experimental step was practically the same but now we placed a focused incoherent light beam of a LED using a convergent lens with a focal length of 20 mm. This configuration ensures full and homogeneous coverage of the HOTSH PhC by the 400-nm LED radiation. Again, we focused the laser radiation of  $\lambda = 1550$  nm on the HOTSH PhC now also bathed with an incoherent 400-nm light beam that deteriorates the coupling as depicted in the blue dots curve shown in Fig. 5(c). Here it can be seen that the coupling of the laser radiation at the interface of the HOTSH PhC no longer occurs, which is reflected in the absence of the peak in the coupling curve. Similarly, in Fig. 5(d), we present the coupling curve (continuous blue line) obtained from the numerical simulations where there is also no peak related to the gapped edge state when we assume a 400-nm illumination. Note that in the numerical simulations that include the change in refractive index with 400-nm LED illumination, we use only the  $\Delta n = -0.02$  obtained from Eqs. (5)–(8). Of note, as shown in Figs. 5(c) and 5(d), the experimental results agree remarkably well with the theoretical results. We have calculated that the percentage of agreement between the experimental and theoretical results is 97% when the edge state is not suppressed. While for the case where the edge state is suppressed with incoherent LED illumination, the percentage of agreement is 88.4%. We attribute that the excellent agreement between numerical and experimental results is due to the fact that the edge states in the HOTSH PhC are gapped, so they cannot degenerate with the bulk states. In addition, the geometrical parameters of the PhC are straightforward to achieve, and combined with the topological protection, the agreement between the theoretical and experimental results is generally improved. With this, we demonstrate that the theoretical calculations obtained from the numerical simulations have a significantly elevated level of reliability.

Figure 6 summarizes the results of the switching effect in the HOTSH PhC, showing the cross section of the system where the gapped edge state propagates. When the LED incoherent light is turned OFF [Fig. 6(a)], the edge state propagates freely. On the other hand, when the LED incoherent light is turned ON [Fig. 6(b)], it induces charge-carrier transitions, changing the dielectric permittivity and shifting the frequency of the edge state. For this reason, the frequency of the edge state no longer matches the frequency of the laser beam that previously exited it and cannot propagate at the HOTSH PhC interface. In addition, in Fig. 6(c), we have plotted a graph where the photonic

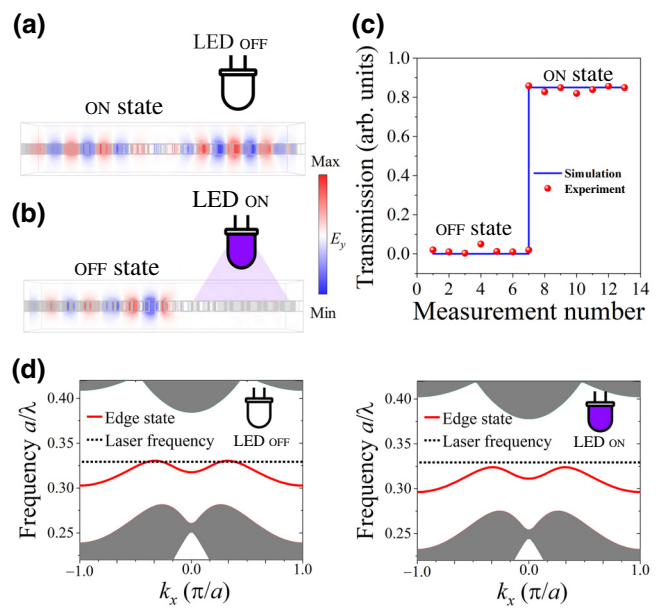


FIG. 6. (a) Cross-section view of the HOTSH PhC showing the  $E_y$ -field distribution of the ON state of the photonic switch. Here the incoherent light source is OFF and no change in dielectric permittivity is generated. (b) Cross-section view of the HOTSH PhC showing the  $E_y$ -field distribution of the OFF state of the photonic switch. Here the incoherent light source is ON and generates charge-carrier transition. (c) Plot of the photonic switch effect realized with the edge state transmission as a function of various experimental and numerically simulated mediations. (d) Comparison of the one-dimensional band-diagram projections for the HOTSH PhC with (right) and without (left) incoherent LED illumination. Here, the band shift in frequencies is shown, causing the laser frequency to no longer intersect the frequency of the gapped edge state.

disruption effect is evident by plotting the transmittance against both experimental and simulated measurements. Finally, in Fig. 6(d), we show the calculation of the photonic band diagram illustrating the mechanism by which the all-optical switch works. This calculation, performed with the change of dielectric permittivity obtained from Eq. (5) and our experimental data, confirms the original hypothesis about the frequency shift of the gapped edge state by incoherent LED illumination. Therefore, the laser cannot couple to the topological interface, and the abrupt decay of the transmittance occurs.

The results obtained in the present research demonstrate that the device designed and built by FIB techniques can generate a guided light beam in a perpendicular direction to a driving light beam, in one telecommunications band (1550 nm), working under the HOTSH effect. As has been shown, the incoherent violet light beam pump changes the dielectric permittivity by the induction of free charge-carrier transition and deteriorates the coupling between the driving coherent light beam and the topological edge state in the PhC device, providing the all-optical switch effect.

#### IV. CONCLUSIONS

Summarizing, in this work we have shown theoretically and experimentally that topological HOTSH PhCs present manipulable edge states, especially useful for generating all-optical switching devices. We have found through numerical simulations that the HOTSH PhC proposed in this work presents a topological phase transition, which confers to the system gapped edge states in the middle of the photonic band gap. Interestingly, although the edge states are robust to structural defects, they are easily manipulated by changes in the refractive index. We have succeeded in manipulating the edge states by exciting free carriers in Si using electromagnetic incoherent radiation with a pump beam energetic enough to overcome the band-gap energy of silicon. Using a 400-nm wavelength beam, we change the dielectric permittivity of the Si slab on which the HOTSH PhC is designed, which changes the frequency of the edge state inside the photonic band gap. These results were experimentally verified by fabricating the HOTSH PhC using only the FIB milling technique and the respective optical characterization through transmittance techniques. For the experimental measurement methodology, we tuned the structural parameters of the HOTSH PhC to obtain the edge state at 1550-nm wavelength, one of the most significant bands in telecommunications, and we demonstrated that the switching effect occurs through a 91% decrease in transmittance. Since both the passive operation (transmission of the gapped edge state) and the active operation (induction of charge carrier transition) are due purely to optical effects, the overall operation of the photonic switch is all optical. The photonic structure studied here is fully compatible with current semiconductor fabrication techniques and operates in a telecommunications band. The present results are of technological significance for the generation of future applied photonic devices in classical and quantum computation.

#### ACKNOWLEDGMENTS

The authors want to thank Centro de Investigación en Materiales Avanzados (CIMAV) for providing the resources required to develop this research. José A. Medina-Vázquez and Evelyn Y. González-Ramírez, want to thank the Consejo Nacional de Ciencia y Tecnología (CONAHCyT) for the Scholarship Grants No. 866231 and No. 866214 provided to develop this research. José G. Murillo Ramírez would like to thank CONAHCyT México for complementary support from “Estancias Sabáticas Vinculadas a la Consolidación de Grupos de Investigación.”

- [2] S. John, Strong localization of photons in certain disordered dielectric superlattices, *Phys. Rev. Lett.* **58**, 2486 (1987).
- [3] J. D. Joannopoulos, P. R. Villeneuve, and S. Fan, Photonic crystals: putting a new twist on light, *Nature* **386**, 143 (1997).
- [4] Z. A. Zaky, M. R. Singh, and A. H. Aly, Tamm resonance excited by different metals/graphene, *Photonics Nanostruct.* **49**, 100995 (2022).
- [5] A. H. Aly and Z. A. Zaky, Ultra-sensitive photonic crystal cancer cells sensor with a high-quality factor, *Cryogenics* **104**, 102991 (2019).
- [6] A. H. Aly, A. A. Ameen, M. A. Mahmoud, Z. S. Matar, M. Al-Dossari, and H. A. Elsayed, Photonic crystal enhanced by metamaterial for measuring electric permittivity in GHz range, *Photonics* **8** (10), 416 (2021).
- [7] A. H. Aly, Z. A. Zaky, A. S. Shalaby, A. M. Ahmed, and D. Vigneswaran, Theoretical study of hybrid multifunctional one-dimensional photonic crystal as a flexible blood sugar sensor, *Phys. Scr.* **95**, 035510 (2020).
- [8] Z. A. Zaky and A. H. Aly, Novel smart window using photonic crystal for energy saving, *Sci. Rep.* **12**, 1 (2022).
- [9] M. T. Tamman, Z. A. Zaky, A. Sharma, Z. S. Matar, A. Aly, and M. A. Mohaseb, Defected photonic crystal array using porous GaN as malaria sensor, *IOP Conf. Ser.: Mater. Sci. Eng.* **1171**, 012005 (2021).
- [10] C. L. Kane and E. J. Mele,  $Z_2$  topological order and the quantum spin Hall effect, *Phys. Rev. Lett.* **95**, 146802 (2005).
- [11] C. L. Kane and J. Mele, Quantum spin Hall effect in graphene, *Phys. Rev. Lett.* **95**, 226801 (2005).
- [12] J. E. Moore, The birth of topological insulators, *Nature* **464**, 194 (2010).
- [13] A. B. Bernevig and T. L. Hughes, *Topological Insulators and Topological Superconductors* (Princeton University, Princeton, 2013).
- [14] G. J. Ferreira and D. Loss, Magnetically defined qubits on 3D topological insulators, *Phys. Rev. Lett.* **111**, 106802 (2013).
- [15] F. Katmis, V. Lauter, F. S. Nogueira, B. A. Assaf, M. E. Jamer, P. Wei, B. Satpati, J. W. Freeland, I. Eremin, D. Heiman, P. Jarillo-Herrero, and J. S. Moodera, A high-temperature ferromagnetic topological insulating phase by proximity coupling, *Nature* **533**, 513 (2016).
- [16] G. Jotzu, M. Messer, R. Desbuquois, M. Lebrat, T. Uehlinger, D. Greif, and T. Esslinger, Experimental realization of the topological Haldane model with ultracold fermions, *Nature* **515**, 237 (2014).
- [17] Y. Hatsugai, Chern number and edge states in the integer quantum Hall effect, *Phys. Rev. Lett.* **71**, 3697 (1993).
- [18] X. Huang, Y. Lai, Z. Hang, and C. T. Chang, Dirac cones induced by accidental degeneracy in photonic crystals and zero-refractive-index materials, *Nat. Mater.* **10**, 582 (2011).
- [19] W.-J. Chen, S.-J. Jiang, X.-D. Chen, B. Zhu, L. Zhou, J.-W. Dong, and C. T. Chan, Experimental realization of photonic topological insulator in a uniaxial metacrystal waveguide, *Nat. Commun.* **5**, 5782 (2014).
- [20] D. Borges-Silva, C. H. Costa, B. R. Carvalho, and C. G. Bezerra, Pseudospin topological behavior and topological edge states in a two-dimensional photonic crystal composed of Si rods in a triangular lattice, *Phys. Rev. B* **107**, 075406 (2023).

[1] E. Yablonovitch, Inhibited spontaneous emission in solid-state physics and electronics, *Phys. Rev. Lett.* **58**, 2059 (1987).

- [21] X. Cheng, C. Jouvaud, X. Ni, S. H. Mousavi, A. Z. Genack, and A. B. Khanikaev, Robust reconfigurable electromagnetic pathways within a photonic topological insulator, *Nat. Mater.* **15**, 542 (2016).
- [22] A. Slobozhanyuk, A. V. Shchelokova, X. Ni, S. Hossein Mousavi, D. A. Smirnova, P. A. Belov, A. Alù, Y. S. Kivshar, and A. B. Khanikaev, Near-field imaging of spin-locked edge states in all-dielectric topological metasurfaces, *Appl. Phys. Lett.* **114**, 031103 (2019).
- [23] D. J. Bisharat and D. F. Sievenpiper, Electromagnetic-dual metasurfaces for topological states along a 1D interface, *Laser Photonics Rev.* **13**, 1900126 (2019).
- [24] L. Zhang, Y. Yang, M. He, H.-X. Wang, Z. Yang, E. Li, F. Gao, B. Zhang, R. Singh, J.-H. Jiang, and H. Chen, Valley kink states and topological channel intersections in substrate-integrated photonic circuitry, *Laser Photonics Rev.* **13**, 1900159 (2019).
- [25] L. Lu, J. D. Joannopoulos, and M. Soljačić, Topological photonics, *Nat. Photonics* **8**, 821 (2014).
- [26] D. Song, V. Paltoglou, S. Liu, Y. Zhu, D. Gallardo, L. Tang, J. Xu, M. Ablowitz, N. K. Efremidis, and Z. Chen, Unveiling pseudospin and angular momentum in photonic graphene, *Nat. Commun.* **6**, 6272 (2015).
- [27] Y. Kang, X. Ni, X. Cheng, A. B. Khanikaev, and A. Z. Genack, Pseudo-spinvalley coupled edge states in a photonic topological insulator, *Nat. Commun.* **9**, 3029 (2018).
- [28] X. D. Chen, Z. L. Deng, W. J. Chen, J. R. Wang, and J. W. Dong, Manipulating pseudospin-polarized state of light in dispersion-immune photonic topological metacrystals, *Phys. Rev. B* **92**, 014210 (2015).
- [29] O. Hosten and P. Kwiat, Observation of the spin Hall effect of light via weak measurements, *Science* **319**, 787 (2008).
- [30] X. Yin, Z. Ye, J. Rho, Y. Wang, and X. Zhang, Photonic spin Hall effect at metasurfaces, *Science* **339**, 1405 (2013).
- [31] Y. Yang, Y. F. Xu, T. Xu, H.-X. Wang, J.-H. Jiang, X. Hu, and Z. H. Hang, Visualization of a unidirectional electromagnetic waveguide using topological photonic crystals made of dielectric materials, *Phys. Rev. Lett.* **120**, 217401 (2018).
- [32] L. H. Wu and X. Hu, Scheme for achieving a topological photonic crystal by using dielectric material, *Phys. Rev. Lett.* **114**, 223901 (2015).
- [33] K. Y. Bliokh, D. Smirnova, and F. Nori, Quantum spin Hall effect of light, *Science* **348**, 1448 (2015).
- [34] F. D. M. Haldane and S. Raghu, Possible realization of directional optical waveguides in photonic crystals with broken time-reversal symmetry, *Phys. Rev. Lett.* **100**, 013904 (2008).
- [35] Z. Wang, Y. Chong, J. D. Joannopoulos, and M. Soljacic, Observation of unidirectional backscattering immune topological electromagnetic states, *Nature* **461**, 772 (2009).
- [36] M. Hafezi, S. Mittal, J. Fan, A. Migdall, and J. M. Taylor, Imaging topological edge states in silicon photonics, *Nat. Photonics* **7**, 1001 (2013).
- [37] A. B. Khanikaev, S. H. Mousavi, W.-K. Tse, M. Kargarian, A. H. MacDonald, and G. Shvets, Photonic topological insulators, *Nat. Mater.* **12**, 233 (2013).
- [38] Y. Zhao, F. Liang, X. Wang, D. Zhao, and B.-Z. Wang, Tunable and programmable topological valley transport in photonic crystals with liquid crystals, *J. Phys. D: Appl. Phys.* **55**, 155102 (2022).
- [39] A. B. Khanikaev and G. Shvets, Two-dimensional topological photonics, *Nat. Photonics* **11**, 763 (2017).
- [40] M. C. Rechtsman, J. M. Zeuner, Y. Plotnik, Y. Lumer, D. Podolsky, F. Dreisow, S. Nolte, M. Segev, and A. Szameit, Photonic Floquet topological insulators, *Nature* **496**, 196 (2013).
- [41] L. Xu, H.-X. Wang, Y.-D. Xu, H.-Y. Chen, and J.-H. Jiang, Accidental degeneracy and topological phase transitions in two-dimensional core-shell dielectric photonic crystals, *Opt. Express* **24**, 18059 (2016).
- [42] W. A. Benalcazar, T. Li, and T. L. Hughes, Quantization of fractional corner charge in Cn-symmetric higher-order topological crystalline insulators, *Phys. Rev. B* **99** (24), 245151 (2019).
- [43] J. A. Medina-Vázquez, Influence of asymmetric long-range interactions on corner states in photonic higher-order topological insulators, *Phys. Rev. A* **107**, 043503 (2023).
- [44] José A. Medina-Vázquez, Evelyn Y. González-Ramírez, and José G. Murillo-Ramírez, Corner states in photonic higher-order Dirac semimetals, *Phys. Rev. A* **107**, 053511 (2023).
- [45] José A. Medina-Vázquez, José G. Murillo-Ramírez, Evelyn Y. González-Ramírez, and Sion F. Olive-Méndez, Weak and strong coupling regimes in a topological photonic crystal bowtie cavity, *J. Appl. Phys.* **132**, 133104 (2022).
- [46] B. Xie, G. Su, H.-F. Wang, F. Liu, L. Hu, S.-Y. Yu, P. Zhan, M.-H. Lu, Z. Wang, and Y.-F. Chen, Higher-order quantum spin Hall effect in a photonic crystal, *Nat. Commun.* **11**, 3768 (2020).
- [47] Z.-K. Lin, S.-Q. Wu, H.-X. Wang, and J.-H. Jiang, Higher-order topological spin Hall effect of sound, *Chin. Phys. Lett.* **37**, 074302 (2020).
- [48] T. Kampfrath, D. M. Beggs, T. P. White, M. Burresi, D. V. Oosten, T. F. Krauss, and L. Kuipers, Ultrafast rerouting of light via slow modes in a nanophotonic directional coupler, *Appl. Phys. Lett.* **94**, 241119 (2009).
- [49] K. A. Aly, Comment on the relationship between electrical and optical conductivity used in several recent papers published in the journal of materials science: materials in electronics, *J. Mater. Sci: Mater. Electron.* **33**, 2889 (2022).
- [50] A. Opheij, N. Rotenberg, D. M. Beggs, I. H. Rey, T. F. Krauss, and L. Kuipers, Ultracompact (3 μm) silicon slow-light optical modulator, *Sci. Rep.* **3**, 3546 (2013).
- [51] B.-Y. Xie, H.-F. Wang, H.-X. Wang, X.-Y. Zhu, J.-H. Jiang, M.-H. Lu, and Y.-F. Chen, Second-order photonic topological insulator with corner states, *Phys. Rev. B* **98**, 205147 (2018).
- [52] C. Schinke, P. C. Peest, J. Schmidt, R. Brendel, K. Bothe, M. R. Vogt, I. Kröger, S. Winter, A. Schirmacher, S. Lim, H. T. Nguyen, and D. MacDonald, Uncertainty analysis for the coefficient of band-to-band absorption of crystalline silicon, *AIP Adv.* **5**, 067168 (2015).
- [53] K. Sokolowski-Tinten and D. von der Linde, Generation of dense electron-hole plasmas in silicon, *Phys. Rev. B* **61**, 2643 (2000).
- [54] R. Bruck, B. Mills, B. Troia, D. J. Thomson, F. Y. Gardes, Y. Hu, G. Z. Mashanovich, V. M. N. Passaro, G. T. Reed, and O. L. Muskens, Device-level characterization of the flow of light in integrated photonic circuits using ultrafast photomodulation spectroscopy, *Nat. Photonics* **9**, 54 (2015).